applied sciences

MDPI

Article

A Real-Time Simulator for an Innovative Hybrid Thermal Management System Based on Experimental Verification

Yu-hsuan Lin [1], Li-fan Liu [2], Yi-hsuan Hung [3,*] and Chun-hsin Chang [3]

[1] Department of Power Mechanical Engineering, National Tsing Hua University, Hsinchu City 300, Taiwan; s107033801@m107.nthu.edu.tw
[2] Department of Industrial Education, National Taiwan Normal University, Taipei City 106, Taiwan; leslie86615@gmail.com
[3] Program of Vehicle and Energy Engineering, National Taiwan Normal University, Taipei City 106, Taiwan; cchsin@ntnu.edu.tw
* Correspondence: hungyh@ntnu.edu.tw; Tel.: +886-2-7749-6494

Featured Application: This innovative hybrid thermal management system is able to be widely applied in electric vehicles with dual energy sources for the purpose of maintaining the optimal temperatures and efficiencies.

Abstract: The performance and efficiency of green energy sources in electric vehicles (EVs) are significantly affected by operation temperatures. To maintain the optimal temperatures of a hybrid energy system (HES), an innovative hybrid thermal management system (IHTMS) was designed. The IHTMS contains a coolant pump, a heat exchanger, a proportional valve for hybrid flow rates, five coolant pipes, and three electromagnetic valves to form two mode-switch coolant loops. A Matlab/Simulink-based simulator of the IHTMS was constructed by formulating a set of first-ordered dynamics of temperatures of coolant pipes and energy bodies using the theories of Newton's law of cooling and the lumped-parameter technique. Parameters were majorly derived by measured performance maps and data from the experimental platform of the IHTMS. To properly manage the optimal temperatures, four control modes were designed for inner-loop form and outer-loop form. For the experimental platform to verify the simulator, two power supplies generated the waste heat of dual energy sources calculated by the driving cycle and vehicle dynamics. Simulation results show that the temperatures were controlled at their optimal ranges by proper mode/loop switch. With the inner-loop mechanism, the rise time of optimal temperature decreased 27.4%. The average simulation-experiment temperature error of the battery was 0.898 °C; the average simulation-experiment temperature error of the PEMFC was 4.839 °C. The IHTMS will be integrated to a real HES in the future.

Keywords: fuel cell; battery; electric vehicle; thermal management system; control strategy

Citation: Lin, Y.-h.; Liu, L.-f.; Hung, Y.-h.; Chang, C.-h. A Real-Time Simulator for an Innovative Hybrid Thermal Management System Based on Experimental Verification. *Appl. Sci.* **2021**, *11*, 11729. https://doi.org/10.3390/app112411729

Academic Editor: Muhammad Aziz

Received: 22 October 2021
Accepted: 6 December 2021
Published: 10 December 2021

1. Introduction

To decrease the usage of fossil fuels so that the greenhouse effect can be eased up, several green energy sources have been widely applied to transportation and power stations. For instance, some study developed the mathematical model of gas-to-power, power-to-gas, power-to-hydrogen (electrolysis), and hydrogen-to-gas (methanation) to simulate the energy management and conversion. The measured data have been compared to the simulation results and have shown the precision model conducted in this research [1]. For green vehicles, these zero-emission energy sources have been used for battery electric vehicles (BEVs), hybrid electric vehicles (HEVs), and fuel cell hybrid vehicles (FCHVs) for the reduction of air pollutants. However, the high C-rate charge/discharge, the low-temperature operation and the low state-of-charge (SOC) of lithium batteries might cause serious problems such as: thermal runaway, capacity fade (aging), high inner resistance

and lithium dendrite formation [2]. Similarly, for the proton exchange membrane fuel cells (PEMFCs), to protect the systems, several issues are required to be concerned: keeping 60–80 °C operation temperature, thickness of membrane, humidity of membrane and reaction gas pressures [3]. From the above, the improvement of these concerns, especially for the temperature control (thermal management), the cooling system will enhance the charge/discharge efficiency, and extend the life cycle of the energy sources so that the green vehicle performance will be raised.

Meanwhile, the concept of "hybridization", which was proposed recently, has been successfully employed to several vehicles such as EVs and HEVs. For example, a three-power-source hybrid powertrain was developed, and a proposed optimal control of integrated energy management/mode switch timing led to significant energy and CO_2 reduction [4]. For dual in-wheel motors (IWMs) designs for EVs, the global search method (GSM) was used for optimal control strategies and motor sizing selection [5]. For the comparison of control strategies of hydrogen fuel cell vehicles, the equivalent consumption minimization strategy (ECMS), peaking power source strategy and fuzzy logic control strategy (FLCS) were used to compensate the inherent drawbacks of lower power density and less power response of fuel cells [6]. It proved that the ECMS increased the operation efficiency, reduces the cost and it decreased the fuel consumption. In this research, an emulated fuel cell/battery hybrid power system was developed while the hybrid thermal control technique was designed.

To efficiently analyze the thermal effect for green energy source prior to experiments, system modeling and numerical simulation are necessary. To minimize aging by adopting the optimal charging strategy, the battery model was built so that the operation conditions (temperature, aging, state-of-charge) were input and the optimal fast charging was selected [7]. A thermal model of full-size-scale cylindrical battery pack cooled by channeled liquid flow was developed [8]. For another study, the charging and discharging C-rate (2 C, 1 C or 0.5 C) were given for simulation and experimental verification. The study reviewed the factors (i.e., high C-rate charge/discharge, aging, etc.) that caused thermal hazards of the lithium-ion battery, and the corresponding countermeasures were proposed [9]. To simulate the thermal management system, a study calculated the thermal behavior of multiple pipes and heat sources. A three-dimensional battery model as well as the thermal management system model were constructed to identify the wear margin of a pipeline [10]. The mini-channel cold-plate was designed while the number of channels, inlet mass flow rate, flow direction, and width of channels were determined [11]. Moreover, a thermoelectric-heat-pump was employed for the dynamic cooling ability distribution of a liquid cooling system. In another study, a combined-cold-plate thermoelectric heat pump was used for managing battery temperatures [12]. In [13], the control strategies, PID, fuzzy-PID, and BP-PID controllers, were compared. The lithium-titanate battery (LTO) thermal model as well as the cooling system were constructed on COMSOL Multiphysics software. By using the forced convection with the sandwiched heat pipes cooling system, the battery temperature was decreased by 33.4% compared to the case of natural convection (56.8 °C to 37.8 °C).

For the experimental studies, a study established the model of off-grid smart homes first by using mixed-integer linear programming, where the optimal electrification was designed. Simulation results showed that the total cost was reduced by 41.5% [14]. For the battery performance affected by the thermal management system, a study proposed the battery aging under various temperatures, cooling approaches, phase change materials, types of coolant pipes, etc. [15]. The thermal performance of a compact battery module under forced convection cooling was studied as well. The system consists of NCR18650 batteries and was used for forced convection test. It proves that the charge/discharge efficiency was increased at 40 °C [16]. In another study, the experimental analysis on the thermal management of lithium-ion batteries based on phase change materials was conducted. It showed that using the phase change materials effectively reduced the temperature by 4 °C compared to the natural convection [17]. For the nanofluids for cooling, a heat

dissipation system with nanofluids was studied. The weight fractions of nanoparticle were 0.5, 1.0, and 1.5 wt %; the flow rates were 1.8, 2.1, and 2.4 L/min, while the coolant temperatures were 30, 40, 50, and 60 °C. It showed that 40% heat dissipation was improved at 1.5 wt %/30 °C [18]. Similarly, the multiwalled carbon nanotube nanofluids were used for heat dissipation system in a hybrid heat source system, and 5% efficiency was improved [19]. The mechatronics design and experimental verification of an electric-vehicle-based hybrid thermal management system was developed [20]. A proportional valve distributed the coolant for governing the operation temperatures of dual energy sources to approach the efficient working areas. The temperature characteristics of an air-cooled proton exchange membrane fuel cell stack were studied. By investigating the temperature distribution, it was found that the surface temperature was within 53–62 °C at output currents of 25–30 A [21]. The thermal performance of a radiator using nanofluids for proton exchange membrane fuel cells (PEMFCs) applications was studied. The Zinc Oxide (ZnO) and Aluminum Nitride (AlN) nanofluids were used for experiments where 10+% heat transfer coefficient value compared with that of water was increased [22]. A thermal equivalent circuit model of heat pipe-based thermal management system for a battery module was developed based on the experiments. It showed that the dynamics between the model and real system were similar [23]. The cold-start performance of fuel cell electric vehicles with heat pump-assisted thermal management systems was analyzed. It showed that 27.3–30.7% of cold-start time was saved [24]. A hybrid carbon nanofluids was used in an air-cooled heat exchanger. Experiments showed that the heat dissipation capability compared with water was improved [25].

In this study, a set of low-ordered dynamics equations for the innovative thermal management system as well as the green energy sources were developed. Meanwhile, the simulator was compared with the mechatronics platform for further controller designs and system verifications. In this research, Section 2 describes the innovative system configuration, dynamics equations, and the construction of the simulator. Section 3 explains how to establish the experimental platform of the hybrid thermal management system. Next, Section 4 discusses the dynamics simulation and experimental results of the Intelligent Hybrid Thermal Management System (IHTMS). Section 5, the Conclusion, summarizes the contributions and future works.

2. Innovative System Configuration, Dynamics Equations, and the Simulator

2.1. Innovative System Configuration

The main concept of the IHTMS was retrieved from the hybrid electric vehicle (HEV) and an internal combustion engine (ICE). The powertrain of a HEV consists of an engine and a traction motor that required the hybrid power distribution to properly and efficiently drive the vehicle. The concept of power distribution was extended to the hybrid coolant flow distribution so that the optimal operation temperatures were remained. From the concept of the ICE cooling system, two coolant-loop paths were switched in the system depending on whether the system reached the target temperature or not. Figure 1 demonstrates the IHTMS for two heat sources with only one cooling system to significantly reduce the cost, occupied space and mass compared to two cooling systems. It consists of five coolant pipes, a heat exchange, a coolant pump, a proportional valve and three electromagnetic valves. The heat exchanger dissipated the coolant heat with a controllable cooling fan; the coolant pump determined the coolant mass flow rate, while the proportional valve properly distributed the flow rates to heat source 1 and heat source 2, respectively, for optimal operation. The coolant brought the waste heat from two heat sources and was sent to one of the two paths: the inner loop and the outer loop by controlling three electromagnetic valves depending on the temperatures of two heat sources. Hence, the IHTMS was characterized by fast response, low occupied volume for EVs or HEVs, and good control for high-efficiency temperatures.

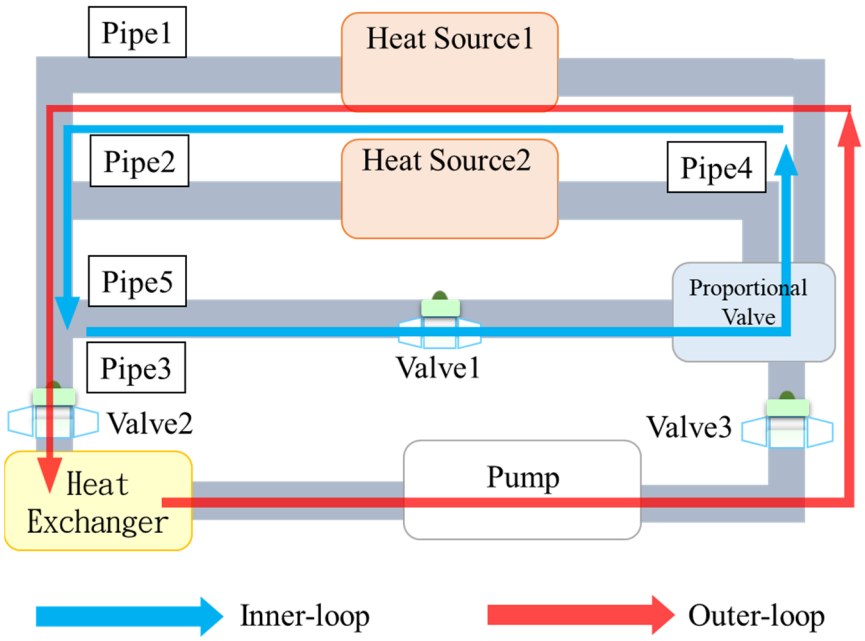

Figure 1. System configuration of the innovative IHTMS designs.

2.2. System Dynamics Equations

2.2.1. Basic Thermal Dynamics of a Control Volume

To construct the control-oriented simulator, the lumped-parameter and low-ordered dynamics of the thermal system were established. The dynamics equations were separated into two types: the coolant pipe and the heat source body. First of all, in the thermal dynamics field, a control volume is defined to be the surface of a volume that allows the mass and energy input and output. For the control volume of a coolant pipe as shown in Figure 2a, based on energy conservation and Newton's law of cooling, a first-ordered dynamic equation was derived as:

$$\dot{T}_i = \frac{\dot{m}_{in} C_{v,w}(\Delta T) - \dot{m}_{out} C_{v,w}(\Delta T) + h_{b,i} A_{b,i}(\Delta T)}{\rho_i V_i C_{v,w}} \tag{1}$$

where T was the lumped temperature; $\dot{m}$, C_v, h, A, ρ, V were the mass flow rate, specific heat at constant volume, heat transfer coefficient, surface area, density, and control volume, respectively. The subscripts i, in, out, amb, and w represent the ith control volume, input, output, ambient and water, respectively. For a control volume of a heat source body, the heat transfer is shown in Figure 2b. Similarly, based on the energy conservation and Newton's law of cooling, a first-order dynamics equation was formulated:

$$\dot{T}_{b,j} = \frac{\dot{Q}_j - h_{w,j} A_{w,j}(\Delta T) - h_{b,j} A_{b,amb}(\Delta T)}{\rho_j V_j C_{v,j}} \tag{2}$$

where $\dot{Q}$ was the generated waste heat power; subscripts b, j were body and the jth heat source. With the above two governing equations, the control-oriented model of the IHTMS can be constructed.

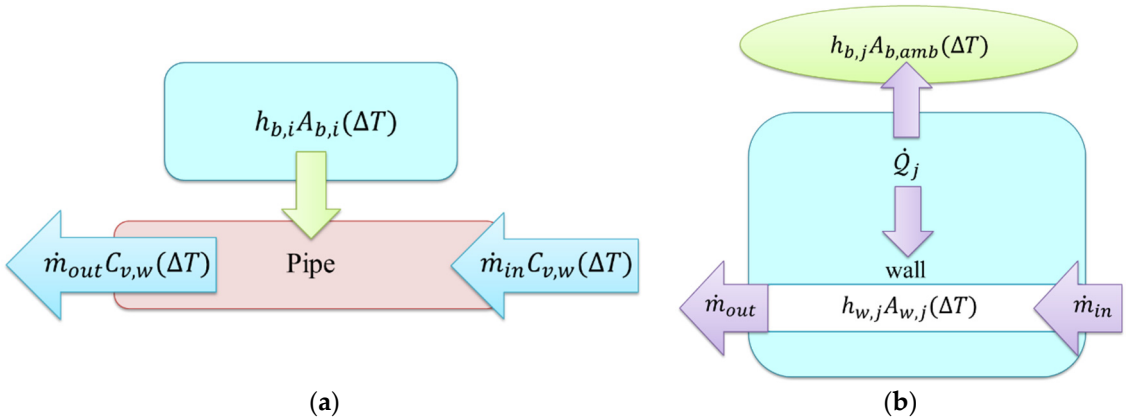

Figure 2. Heat and temperature variation of a control volume: (**a**) coolant pipe, (**b**) body.

2.2.2. Derivation of System Dynamics Equations

According to Figure 1 and Equations (1) and (2), the IHTMS was decomposed into eight control volumes of coolant pipes and two heat source bodies, as illustrated in Figure 3.

(1) Pipe 1: the pipe 1 was defined as a pipe interconnected to the output of the fuel cell coolant channel and the input of pipe 3. The input energy was from the heated coolant from the fuel cell, while the output energy was delivered to pipe 3. Another heat convection was released to the ambient atmosphere. The dynamics equation was formulated as:

$$\dot{T}_{p1} = \frac{\dot{m}_{fc}C_{v,w}\left(T_{w,fc} - T_{p1}\right) - \dot{m}_{fc}C_{v,w}\left(T_{p1} - T_{P3}\right) - h_{p1}A_{p1}\left(T_{p1} - T_{amb}\right)}{\rho_w V_{w,p1}C_{v,w}} \quad (3)$$

where subscripts *fc*, *w*, *p*1, *p*3 represent fuel cell, water, pipe 1 and pipe 3, respectively.

(2) Pipe 2: similar to pipe 1, pipe 2 was a pipe interconnected to the output of the battery coolant channel and the input of pipe 3. The input energy was from the battery coolant while the output energy was sent to pipe 3. The heat convection was released to the ambient atmosphere as well. The dynamics equation was formulated as:

$$\dot{T}_{p2} = \frac{\dot{m}_{bat}C_{v,w}\left(T_{w,bat} - T_{p2}\right) - \dot{m}_{bat}C_{v,w}\left(T_{p2} - T_{P3}\right) - h_{p2}A_{p2}\left(T_{p2} - T_{amb}\right)}{\rho_w V_{w,p2}C_{v,w}} \quad (4)$$

where subscripts bat, *p*2 represent battery and pipe 2, respectively.

(3) Pipe3: the input of pipe 3 was linked to the outputs of pipe 1 and pipe 2, while the pipe 3 output was at the front of electromagnetic valves of the heat exchanger and pipe 5. The input energy was the summation of output energy of pipe 1 and pipe 2, where the output mass flow rate was the summation of those of pipe 1 and pipe 2 ($\dot{m}_{p3} = \dot{m}_{p1} + \dot{m}_{p2}$). The output energy was sent to the heat exchanger or pipe 5 depending on the status of valve 1 and valve 2. The heat convection to the atmosphere was another energy loss. The dynamics equation was formulated as:

$$\dot{T}_{p3} = \frac{\left[\dot{m}_{fc}C_{v,w}\left(T_{p1}-T_{P3}\right)+\dot{m}_{bat}C_{v,w}\left(T_{p2}-T_{p3}\right)\right]-k_1\dot{m}_{p3}C_{v,w}\left(T_{P3}-T_{he}\right)-k_2\dot{m}_{p3}C_{v,w}\left(T_{P3}-T_{p5}\right)-h_{p3}A_{p3}\left(T_{p3}-T_{amb}\right)}{\rho_w V_{w,p3}C_{v,w}} \quad (5)$$

where k_1 and k_2 were "loop-switch" parameters. If the system was in inner-loop mode, $k_1 = 0$ and $k_2 = 1$; whereas in outer-loop mode, $k_1 = 1$ and $k_2 = 0$. Subscripts *he*, *p*5 stand for heat exchanger and pipe 5, respectively.

(4) Pipe 4: the input of pipe 4 was at the output of the proportional valve, while the outputs were linked to the entrances of the coolant channels of the emulated battery and the fuel cell. The input energy was the output energy from the heat exchanger (outer loop) or from pipe 5 (inner loop), where the output energy (and coolant mass

flow) was separated into two paths: to the battery or to the fuel cell. Still, the heat convection to the atmosphere was another energy loss. The dynamics equation was formulated as:

$$\dot{T}_{p4} = \frac{k_1 \dot{m}_{p5} C_{v,w}\left(T_{he} - T_{p4}\right) - k_2 \dot{m}_{p5} C_{v,w}\left(T_{p5} - T_{p4}\right) - \left[\dot{m}_{fc} C_{v,w}\left(T_{p4} - T_{w,fc}\right) + \dot{m}_{bat} C_{v,w}\left(T_{p4} - T_{w,bat}\right)\right] - h_{p4} A_{p4}\left(T_{p4} - T_{amb}\right)}{\rho_w V_{w,p4} C_{v,w}}. \quad (6)$$

where subscript $p4$ means pipe 4.

(5) Pipe 5: the inputs of pipe 5 were the outputs of valve 1, while the output was the entrance of the proportional valve. The input energy was the output energy from valve 1, where the output energy was delivered to pipe 4. The heat convection to the atmosphere was another energy loss. The dynamics equation was formulated as:

$$\dot{T}_{p5} = \frac{\dot{m}_{p3} C_{v,w}\left(T_{p3} - T_{p5}\right) - \dot{m}_{p5} C_{v,w}\left(T_{p5} - T_{p4}\right) - h_{p5} A_{p5}\left(T_{p5} - T_{amb}\right)}{\rho_w V_{w,p5} C_{v,w}} \quad (7)$$

(6) Fuel cell coolant channel and body: for the fuel cell coolant channel, the coolant temperature was influenced by the input energy from pipe 4, the output energy to pipe 1 and the heat transferred from the system body to the coolant, as shown in Equation (8). For the transient fuel cell body temperature, it was effected by the generated waste heat, the heat convection to the atmosphere, and the heat transferred to the coolant channel, as formulated in Equation (9).

$$\dot{T}_{w,fc} = \frac{\dot{m}_{fc} C_{v,w}\left(T_{p4} - T_{w,fc}\right) - \dot{m}_{fc} C_{v,w}\left(T_{w,fc} - T_{p1}\right) + h_{w,fc} A_{w,fc}\left(T_{b,fc} - T_{w,fc}\right)}{\rho_w V_w C_{v,w}} \quad (8)$$

$$\dot{T}_{b,fc} = \frac{\dot{Q}_{fc} - h_{b,fc} A_{b,fc}\left(T_{b,fc} - T_{w,fc}\right) - h_{fc} A_{b,fc}\left(T_{b,fc} - T_{amb}\right)}{\rho_{fc} V_{fc} C_{v,fc}} \quad (9)$$

where $\dot{Q}$ was the heating power, subscript fc means fuel cell.

(7) Battery coolant channel and body: for the battery coolant channel, its temperature was decided by the input energy from pipe 4 as well, the output energy to pipe 2 and the heat sent from the system body to the coolant channel, as shown in Equation (10). For the battery body temperature, it was influenced by the generated waste heat, the heat convection to the atmosphere, and the heat transferred to the coolant channel expressed in Equation (11):

$$\dot{T}_{w,bat} = \frac{\dot{m}_{bat} C_{v,w}\left(T_{p4} - T_{w,bat}\right) - \dot{m}_{bat} C_{v,w}\left(T_{w,bat} - T_{p2}\right) + h_{w,bat} A_{w,bat}\left(T_{b,bat} - T_{w,bat}\right)}{\rho_w V_w C_{v,w}} \quad (10)$$

$$\dot{T}_{b,bat} = \frac{\dot{Q}_{bat} - h_{b,bat} A_{b,bat}\left(T_{b,bat} - T_{w,bat}\right) - h_{bat} A_{bat}\left(T_{b,bat} - T_{amb}\right)}{\rho_{bat} V_{bat} C_{v,bat}} \quad (11)$$

where subscript bat means battery.

(8) Coolant pump and the heat exchanger: for the outer loop, as valve 2 was switched on, the input energy (coolant mass flow) from pipe 3 flew to the coolant pump and the heat exchanger, where the output energy brought by the coolant was delivered to pipe 4. Note that most of the waste heat was removed by the radiator on the heat exchanger. The temperature dynamics was formulated as:

$$\dot{T}_{he} = \frac{\dot{m}_{p3} C_{v,w}\left(T_{p3} - T_{he}\right) - \dot{m}_{p3} C_{v,w}\left(T_{he} - T_{p4}\right) - \dot{Q}_{he}}{\rho_w V_w C_{v,w}} \quad (12)$$

where subscript *he* represents heat exchanger.

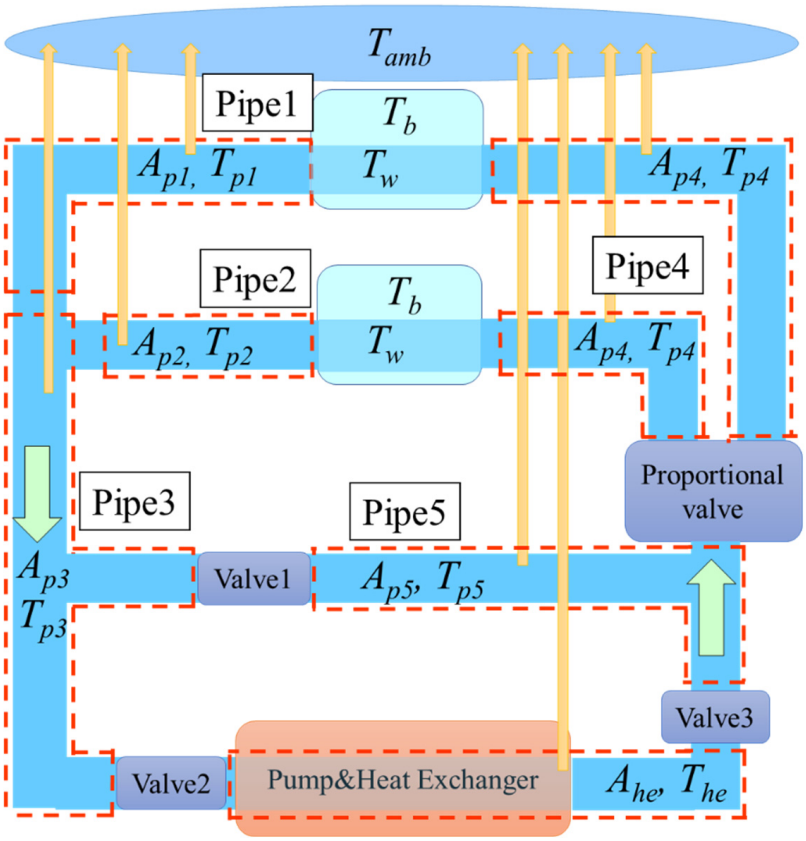

Figure 3. Decomposition of the HTMS.

2.3. Control Strategies for the IHTMS

To manage the optimal temperatures of emulated lithium battery and the PEMFC, the rule-based control strategies were adopted for actuators: electromagnetic valves, proportional valve, electric-controlled radiator, and the coolant pump. The rules were designed as follows:

(a) Electromagnetic valves

If $T_{bat,a} < T_{bat,g}$ and $T_{fc,a} < T_{fc,g}$, $V_{switch} = 0$;
Elseif $T_{bat,a} \geq T_{bat,g}$ and $T_{fc,a} < T_{fc,g}$, $V_{switch} = 0$
Elseif $T_{bat,a} < T_{bat,g}$ and $T_{fc,a} \geq T_{fc,g}$, $V_{switch} = 1$
Elseif $T_{bat,a} > T_{bat,g}$ and $T_{fc,a} > T_{fc,g}$, $V_{switch} = 1$
End

(b) Proportional valve

If $T_{bat,a} < T_{bat,g}$ and $T_{fc,a} < T_{fc,g}$, $V_{pv} = 1.98$;
Elseif $T_{bat,a} \geq T_{bat,g}$ and $T_{fc,a} < T_{fc,g}$,$V_{pv} = 1.8$;
Elseif $T_{bat,a} < T_{bat,g}$ and $T_{fc,a} \geq T_{fc,g}$,
$V_{pv} = V_{pv} + K_{pv} \times \Delta t_{pv}$; $(V_{pv,max} = 3.4)$
Elseif $T_{bat,a} > T_{bat,g}$ and $T_{fc,a} > T_{fc,g}$,
$V_{pv} = V_{pv} + K_{pv} \times \Delta t_{pv}$; $(V_{pv,max} = 3.4)$
End

(c) Electric-controlled radiator

If $T_{bat,a} < T_{bat,g}$ and $T_{fc,a} < T_{fc,g}$, $V_{fan} = 0$;
Elseif $T_{bat,a} \geq T_{bat,g}$ and $T_{fc,a} < T_{fc,g}$,$V_{fan} = 0$;
Elseif $T_{bat,a} < T_{bat,g}$ and $T_{fc,a} \geq T_{fc,g}$,
$V_{fan} = V_{fan} + K_{fan} \times \Delta t_{fan}$; $(V_{pv,max} = 10)$
Elseif $T_{bat,a} > T_{bat,g}$ and $T_{fc,a} > T_{fc,g}$,
$V_{fan} = V_{fan} + K_{fan} \times \Delta t_{fan}$; $(V_{pv,max} = 10)$
End

(d) Coolant pump
If $T_{bat,a} < T_{bat,g}$ and $T_{fc,a} < T_{fc,g}$, $V_{pump} = 1.7$;
Elseif $T_{bat,a} \geq T_{bat,g}$ and $T_{fc,a} < T_{fc,g}$,
$V_{pump} = V_{pump} + K_{pump} \times \Delta t_{pump}$; $(V_{pump,max} = 10)$
Elseif $T_{bat,a} < T_{bat,g}$ and $T_{fc,a} \geq T_{fc,g}$,
$V_{pump} = V_{pump} + K_{pump} \times \Delta t_{pump}$; $(V_{pump,max} = 10)$
Elseif $T_{bat,a} > T_{bat,g}$ and $T_{fc,a} > T_{fc,g}$,
$V_{pump} = V_{pump} + K_{pump} \times \Delta t_{pump}$; $(V_{pump,max} = 10)$
End

where K, Δt, V represent gain, sampling time and voltage, respectively; subscripts a, g, pv, $pump$, fan, $switch$ represent actual, goal, proportional valve, coolant pump, radiator fan, electromagnetic switch, respectively. First of all, four control modes (Mode 1 to Mode 4) were defined in advance. When $T_{bat,a} < T_{bat,g}$ and $T_{fc,a} < T_{fc,g}$, it was in Mode 1. When $T_{bat,a} \geq T_{bat,g}$ and $T_{fc,a} < T_{fc,g}$, it was in Mode 2. As $T_{bat,a} < T_{bat,g}$ and $T_{fc,a} \geq T_{fc,g}$, the operation mode is Mode 3, and Mode 4 is when $T_{bat,a} > T_{bat,g}$ and $T_{fc,a} \geq T_{fc,g}$. The explanations for control strategies were described sequentially: (a) Electromagnetic valves: as Mode 1 or Mode 2, the fuel cell temperature was below the target value, 55 °C. To reach the goal rapidly, $V_{switch} = 0$ leads to the inner-loop mode. As Mode 3 or Mode 4, the system temperature was averagely high so that $V_{switch} = 1$ to enter the outer-loop mode. For (b) Proportional valve: at Mode 1, the proportional valve voltage $V_{pv} = 1.98$, where 75% coolant was sent to the fuel cell while 25% was sent to the battery, so that the two optimal temperatures will be reached nearly simultaneously. When Mode 2 was reached, $V_{pv} = 1.8$ so that more coolant was delivered to the battery and the target fuel cell temperature will be met faster. Contrarily, if the fuel cell temperature exceeded the target value, $V_{pv} = 3.4$ to provide more heat dissipation capacity to the fuel cell. For (c) Electric-controlled radiator: at Mode 1 or Mode 2, since the system temperature was averagely low so that $V_{fan} = 0$; at Mode 3 or Mode 4, because the system temperature was high, the fan activated to remove more waste heat. For (d) Coolant pump: at Mode 1, $V_{pump} = 1.7$ so that the coolant flow rate was 0.4 L/min. as the lowest speed to accelerate the temperature increasing speed. At the other three states, the voltage varied to increase the coolant flow rate. From controlling the above four actuators, the target temperatures will be effectively tracked to reach the optimal operation areas (working temperatures).

2.4. Development of the IHTMS Simulator

The IHTMS simulator was coded on the Matlab/Simulink platform, as shown in Figure 4. For block a, it contains the driving cycles and the derived waste heat governed by the following equations:

$$P_d = \left[M_{veh} V_{veh} + \frac{1}{2} C_d A_{veh} \rho {V_{veh}}^2 + M_{veh} g \cos(\theta) + \mu M_{veh} g \sin(\theta) \right] V_{veh} \quad (13)$$

$$P_{fc} = \frac{P_d}{2};\ P_{bat} = \frac{P_d}{2} \quad (14)$$

$$\dot{Q}_{fc} = \left(1 - \eta_{fc}\right) P_{fc} / \eta_{fc} \quad (15)$$

$$\dot{Q}_{bat} = (1 - \eta_{bat}) P_{bat} / \eta_{bat} \quad (16)$$

where M, C_d, A, ρ, V, g, θ, μ, η represent mass, aero drag coefficient, frontal area, air density, velocity, gravity acceleration constant, climbing degree, rolling resistance coefficient and efficiency, respectively. Subscripts d and veh are demand and vehicle, respectively. Equation (13) was the required vehicle power which was affected by the vehicle acceleration, wind resistance, climbing resistance, and rolling resistance [5]. Equation (14) indicated that the fuel cell and the battery set shared the demanded power equally. Equation (15) determined the waste heat in Equation (9) where the fuel cell efficiency was a function of P_{fc}. Equation (16) determined the waste heat in Equation (11) where the battery effi-

ciency was a function of P_{bat}, battery SOC, and battery inner resistance [4]. For block b, the thermal dynamics of five coolant pipes (pipe 1–5), PEMFC and battery bodies and coolant flow channels according to Equations (3)–(11) was constructed. For block c, it was for the control strategies according to Section 2.3 using the Stateflow toolbox. For block d, it was the inner-loop model; for block e, it was the heat exchanger model derived in Equation (12); for block f, it modeled the proportional valve to separate the coolant flow; for block g, it was the coolant pump model where the coolant flow rate was proportional to the controlled voltage. From the above, Section 2 derives the thermal dynamics of each of the components at first, and the rule-based control was designed next. The integrated system/controlMatlab/Simulink model was coded to evaluate the system performance.

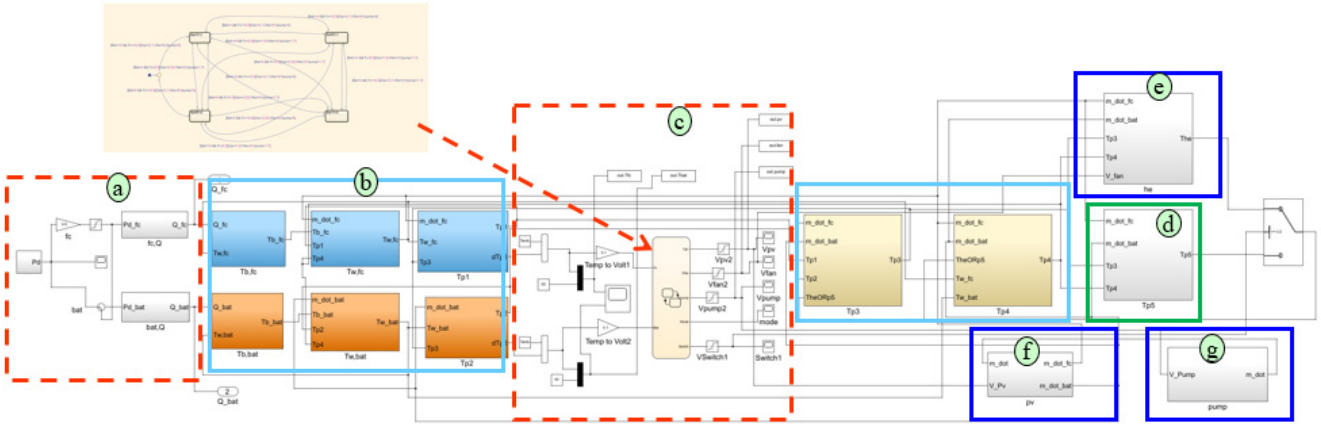

Figure 4. The IHTMS simulator on the Matlab/Simulink platform.

3. Experimental Platform of the Hybrid Thermal Management System

3.1. Hardware Designs of the IHTMS

The hardware design of the ITHMS is shown in Figure 5. The emulated waste heat of dual energy sources was generated by two heaters inserted in two storage tanks (Heat(1) and Heat(2)), where two programmable power supplies provided required instant heating power controlled by LabVIEW on a PC. The inner-loop or outer-loop structure was governed by three electromagnetic valves. The pump and proportional valve determined the coolant flow rates for two heat sources that two flow meters were equipped with before the entrances of Heat(1) and Heat(2). Meanwhile, four temperature sensors before and after Heat(1) and Heat(2) supervised the heat source input–output temperatures. Two other temperature sensors were set at the entrance and exit of the heat exchanger to calculate the heat dissipation capability. An industrial PC with thermal management control strategies received the signals of the temperatures to determine the voltages of the radiator, proportional valve and the coolant pump. A data logger recorded all tested data for further applications. The detailed specifications of the key components are summarized in Table 1.

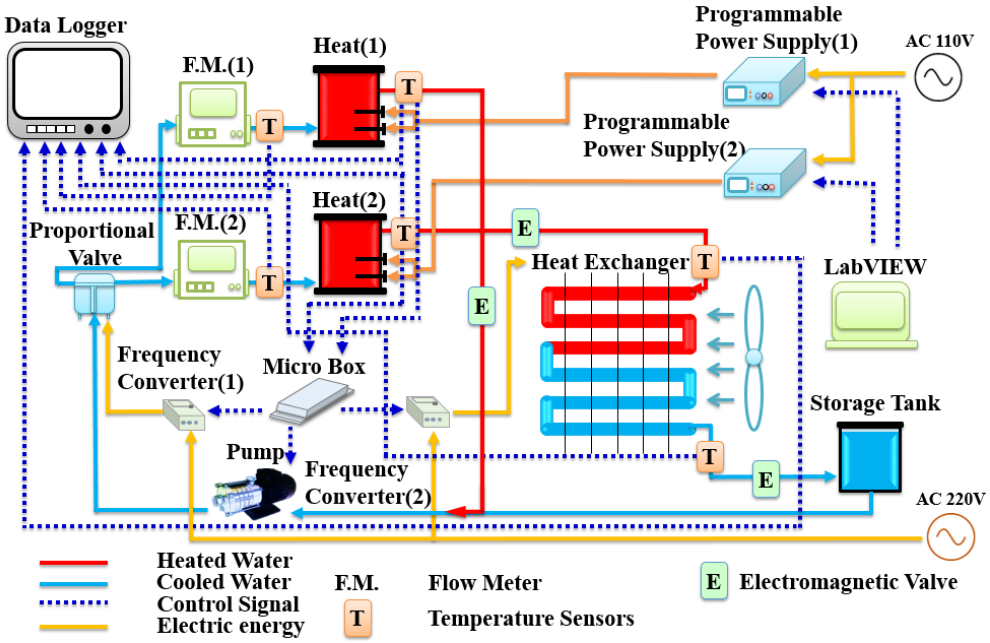

Figure 5. Hardware designs of the IHTMS.

Table 1. Specifications of key components.

Name	Product Model	Specification	Manufacturer
DC Heating Appliance	W	1000 W	Ching-Ta Heating, Taiwan
Programmable Power Supply	PSW80–40.5	1080 W	Good Will Instrument, Taiwan
Temperature Transmitter	TRH-300	0~100 °C	TECPEL, Taiwan
Heat Exchanger	OC-1405	43.18 × 28.57 × 5.7 cm	TECPEL, Taiwan
Coolant Fan	SA12038B2H	113 CFM	STK, Taiwan
Coolant Pump	U85B1	4000 mL/min	United victory scientific, Taiwan
Proportional Valve	AN-01-AMD-360	0~5 V	Anco, Taiwan
Solenoid Valve	1304–15	1/2 in PT	Anco, Taiwan
Micro-Box	Micro-Box 220	–	Terasoft, Taiwan
Variable-frequency Drive	JNTHBCBA0001BE-U-	2HP/1.5 kW	TECO, Taiwan

Figure 6 demonstrates the completed experimental platform of the IHTMS. Label a denotes a PC with LabVIEW system; label b represents two programmable power supplies to provide heating power to the heaters in label c, the two stainless tanks. Label d is the rapid-prototyping controller with the rule-based control strategies. Label e is the proportional valves; label f is the heat exchanger; label g is the coolant pump; label h is the data logger; label i is the AC inverters; label j is the flow meters; label k is the data logger; and label l is the three electromagnetic valves for inner and outer loops. With the arrangement of these key components, the simulation results of the simulator can be compared with the experimental data from the platform in Figure 6.

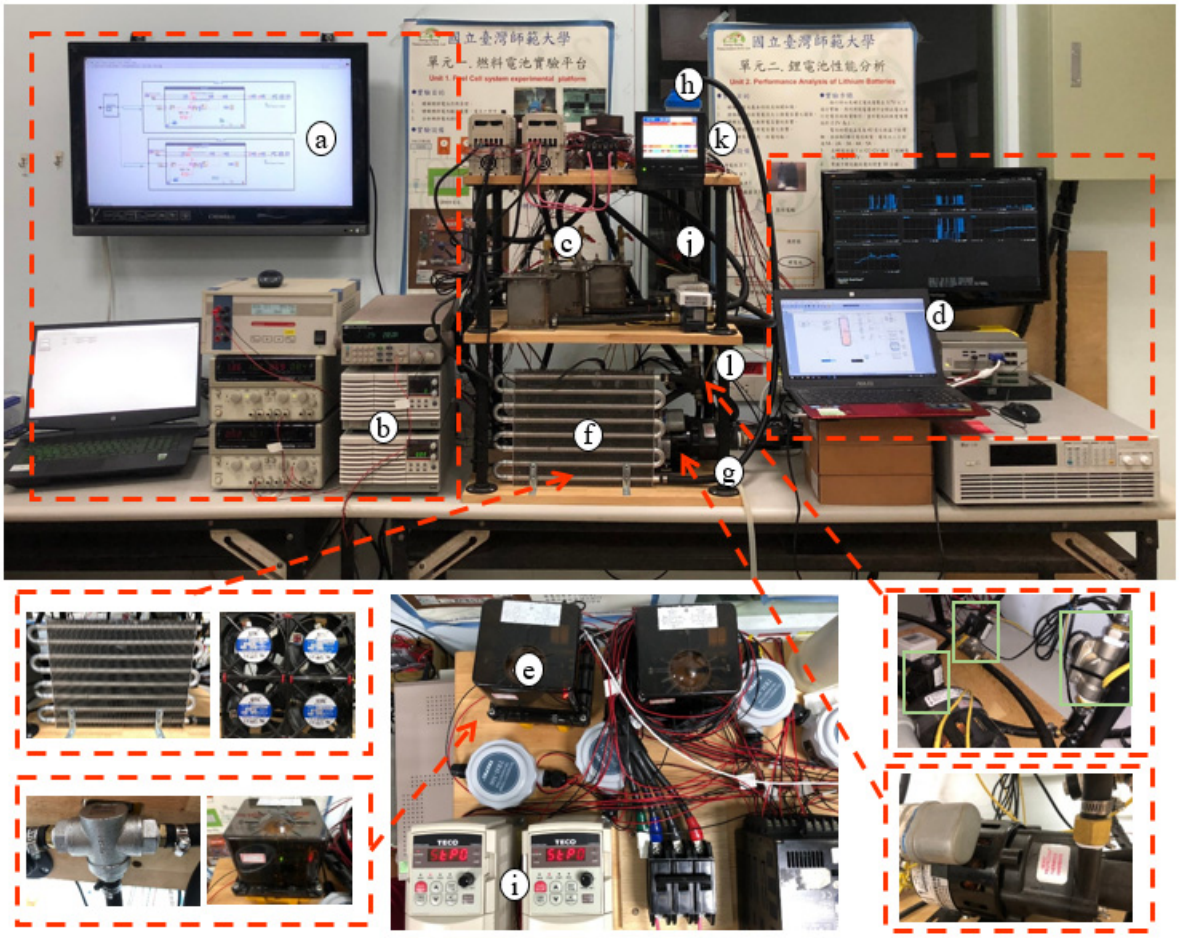

Figure 6. Experimental platform of the IHTMS.

3.2. Control Strategy Designs and Supervision Software

According to Sections 2.3 and 2.4, the waste heat and control strategies were coded in the PC with LabVIEW and the industrial PC (as the controller), respectively. For the waste heat calculation, the Matlab/Simulink model based on Equations (13)–(16) was coded in segment a in Figure 7a. Segment b denotes the input of the LabVIEW. Segment c is the PC for real-time simulation and system supervision. Segment d represents the waste heat commands for LabVIEW. Segment e represents the waste heat commands to the programmable power supply machines; segment f represents two programmable power supply machines, while segment g represents the two heaters receiving the heating power from the power supply machines. For the implementation of control strategies described in Section 2.3, part a in Figure 7b is the Stateflow program that the rule-based control was coded; part b represents the inputs of the system temperatures; part c is the real-time simulator where the rule-based control was operated online. Part d is the controllable proportional valve for coolant flow distribution; part e is the heat exchanger with controllable radiator; part f is the coolant pump; part g denotes three electromagnetic valves for inner-loop and outer-loop control.

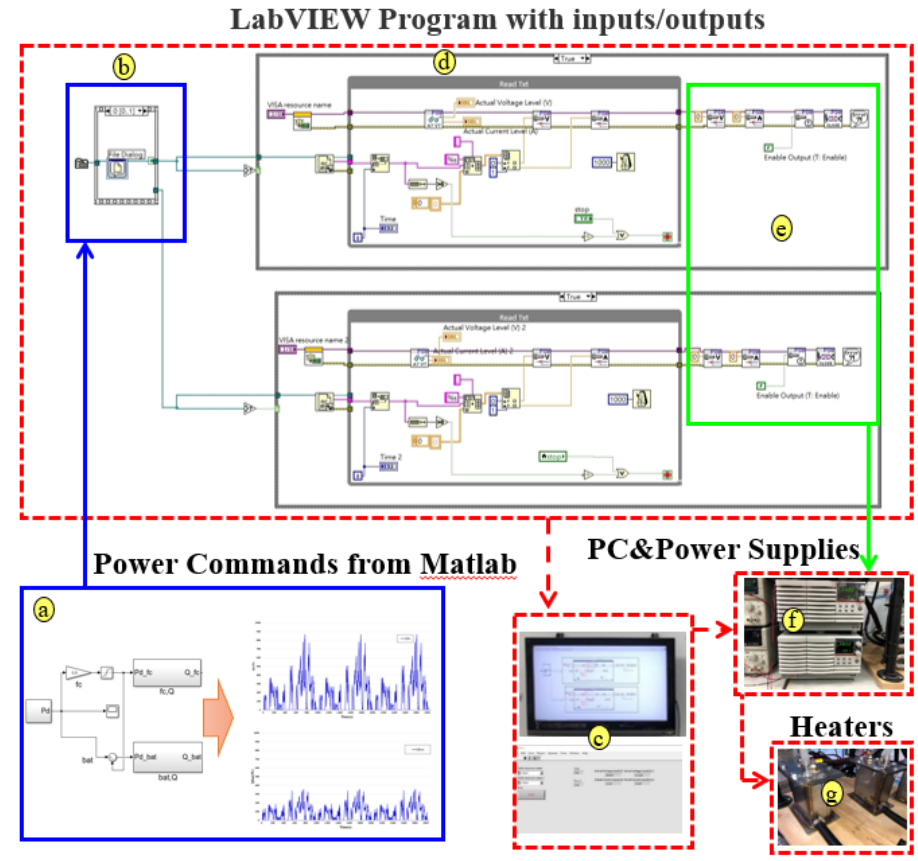

(**a**)

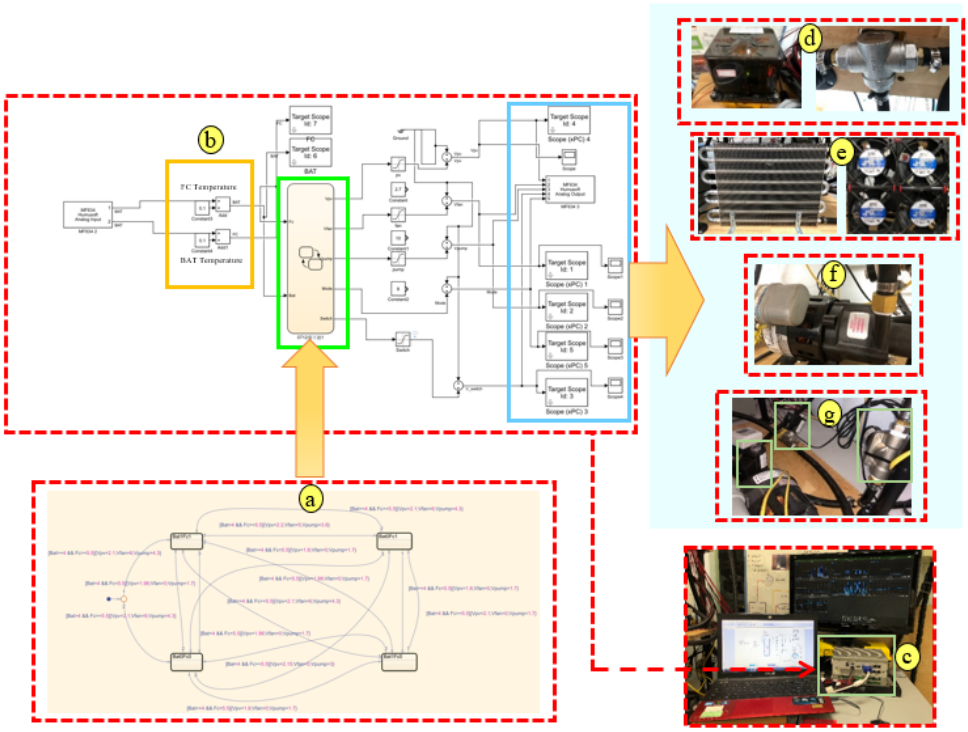

Figure 7. Control and supervision of the IHTMS: (**a**) supervisory software and (**b**) control strategy with applications.

4. Dynamics Simulation and Experimental Results

4.1. Driving Scenarios and Simulator Parameter Setting

Table 2 tabulates the parameters for the IHTMS simulator. It summarizes the parameters from Equations (3)–(12) so that the simulation profiles can be compared with the experimental results. By measuring the surface area of two stainless tanks, A_{fc} and A_{bat} were derived. Since the material of pipe 1–5 was Nitrile Butadiene Rubber (NBR), h_p was given. The pipe surface areas: A_{p1} to A_{p5} were evaluated according to Figure 6. The specific heat at constant volume for the PEMFC and the battery were derived from the simulation software ADVISOR (ADvanced VehIcle SimulatOR).

Table 2. Parameter values of the IHTMS simulator.

Parameters	Symbol (Unit)	Value
Air density	ρ_a (kg/m^3)	1.225
Water density	ρ_w (kg/L)	993
Environment Temperature	T_{amb} (°C)	27
Battery specific heat at constant volume	$C_{v,bat}$ (J/kg K)	759
Fuel cell specific heat at constant volume	$C_{v,fc}$ (J/kg K)	750
Water specific heat at constant volume	$C_{v,w}$ (J/kg K)	4200
Pipe heat transfer coefficient	h_p (m^2 K)	0.25
Inner water channel of Fuel cell heat transfer coefficient	$h_{w,fc}$ (m^2 K)	15
Inner water channel of battery heat transfer coefficient	$h_{w,bat}$ (m^2 K)	15
Fuel cell heat transfer coefficient	h_{fc} (m^2 K)	15
Battery heat transfer coefficient	h_{bat} (m^2 K)	15
Fuel cell surface area	A_{fc} (m^2)	1.5
Battery surface area	A_{bat} (m^2)	1.5
Pipe 1, 2, 4 surface area	$A_{p1,2,4}$ (m^2)	0.2
Pipe 3 surface area	A_{p3} (m^2)	0.25
Pipe 5 surface area	A_{p5} (m^2)	0.3
Water volume	V_w (m^3)	0.004

Table 3 lists the parameters of the vehicle and road conditions for Equations (13)–(16). The proper waste heat of dual energy sources for each time step thus was calculated. Figure 8a is the driving scenario, a standard driving cycle-WLTP (Worldwide harmonized Light vehicles Test Procedure) class 1 was adopted for calculating the waste heat. Figure 8b is the demanded power of dual energy sources evaluated from Equations (13) and (14). Hence, the waste heat of emulated PEMFC and lithium battery is demonstrated in Figure 8c,d. The time-variant waste heat was delivered to the simulator and the experimental platform for the output performance comparison. The assumption of the vehicle mass was 350 kg because we adopted a light EV where the vehicle gross mass is 290 kg. It consists of the fuel cells and hydrogen tanks (50 kg), the lithium battery module with the traction motor and motor controller (60 kg), and the vehicle chassis and frame (180 kg). With one 65 kg driver's weight, the total vehicle mass is 350 kg.

Table 3. Vehicle parameters and road conditions.

Parameter	Symbol (Unit)	Value or Function
Vehicle mass	m_v (kg)	350
Rolling resistance coefficient	μ	0.015
Air drag coefficient	C_d	0.3
Final drive ratio	FR	3.93
Vehicle frontal area	A_{veh} (m^2)	1.5
Gravity	g (m/s^2)	9.81
Road grade	θ(°)	0
Tire radius	Rw (m)	0.254

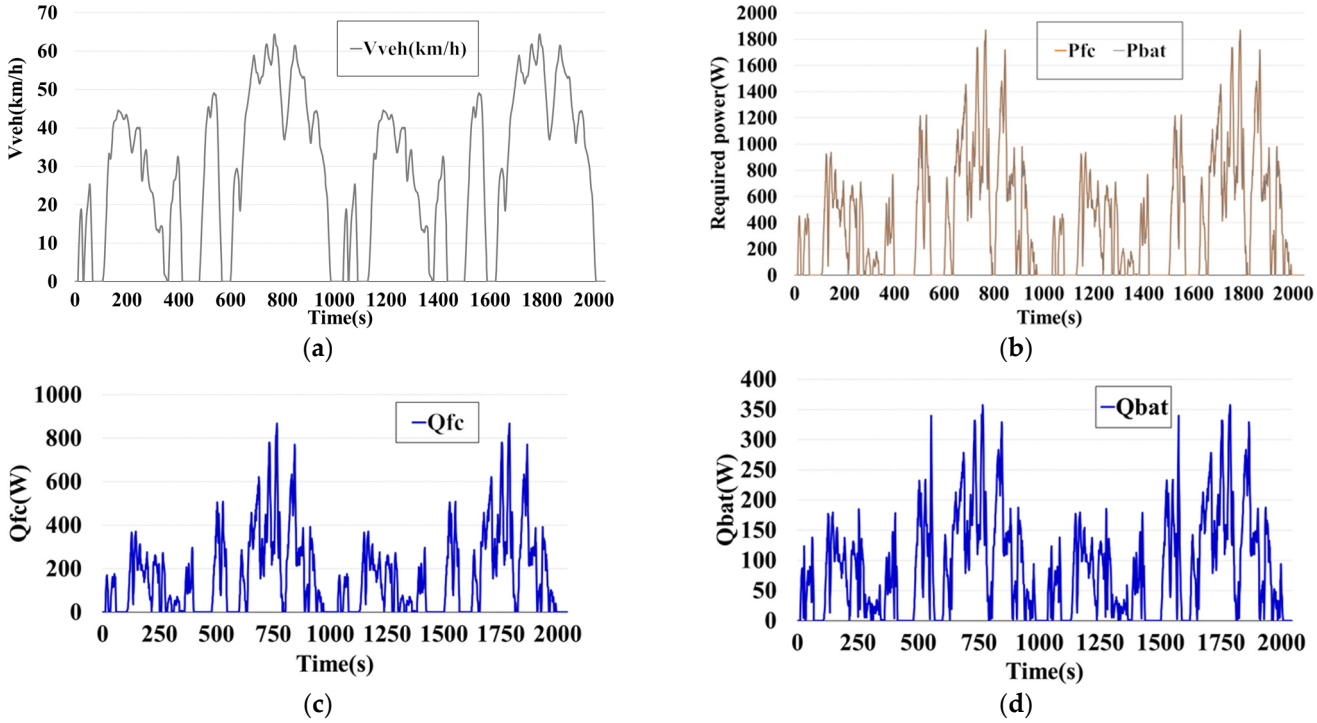

Figure 8. Driving Scenarios with the emulated variables: (**a**) WLTP class 1 driving cycles; (**b**) required power of two energy sources; (**c**) waste heat of emulated PEMFC; (**d**) waste heat of emulated lithium battery.

4.2. Comparison of Simulation and Experimental Results

Figure 9 compares the temperatures of PEMFC and the battery. According to the constructed simulator from Figure 4, and with the waste heat commands from Figure 8c,d, the simulated temperature profiles of the battery system and the PEMFC were plotted. Meanwhile, after the experimental platform was constructed in Figure 6, the experimental temperature profiles were plotted. It shows that for the battery temperature profiles, the simulated one reached the target temperature (40 °C) at the 771st second, while the experimental temperature reached the target at the 876th second. For the PEMFC temperature profiles, the simulated profile reached the target temperature (55 °C) at the 842nd second, while the experimental temperature reached the target at the 684th second. The average simulation-experiment temperature error of the battery was 0.898 °C; the average simulation-experiment temperature error of the PEMFC was 4.839 °C. The average temperature error is defined in Equations (17) and (18):

$$e_{bat} = \frac{\sum_{k=1}^{k=N} \left| T_{bat,sim}(k) - T_{bat,\exp}(k) \right|}{\mathrm{N}} \tag{17}$$

$$e_{fc} = \frac{\sum_{k=1}^{k=N} \left| T_{fc,sim}(k) - T_{fc,\exp}(k) \right|}{\mathrm{N}} \tag{18}$$

where e, N represent error, nth sampling time, respectively. Figure 10 is the simulation/experiment comparison of the mode-switch timing. Mode 1 and mode 2 were in the inner-loop structure, while mode 3 and mode 4 were in the outer-loop structure. For the experimental data, as temperatures of dual sources were under their target values, it was in mode 1. At the 688th second, as investigated from Figure 9 where $T_{bat,a} < T_{bat,g}$ and $T_{fc,a} \geq T_{fc,g}$, the mode was switched to mode 3. After the 1169th second, the system was majorly switched from mode 2 to mode 4. By appropriate mode switch, the system temperatures tracked the targets well. In simulation results, at the 737th second from Figure 9, the battery reached the target temperature while the PEMFC did not, so that

mode 2 was switched. As the PEMFC reached the goal at the 776th second as well, the mode was switched to mode 4, and the system continuously tracked the targets to the end of the simulation.

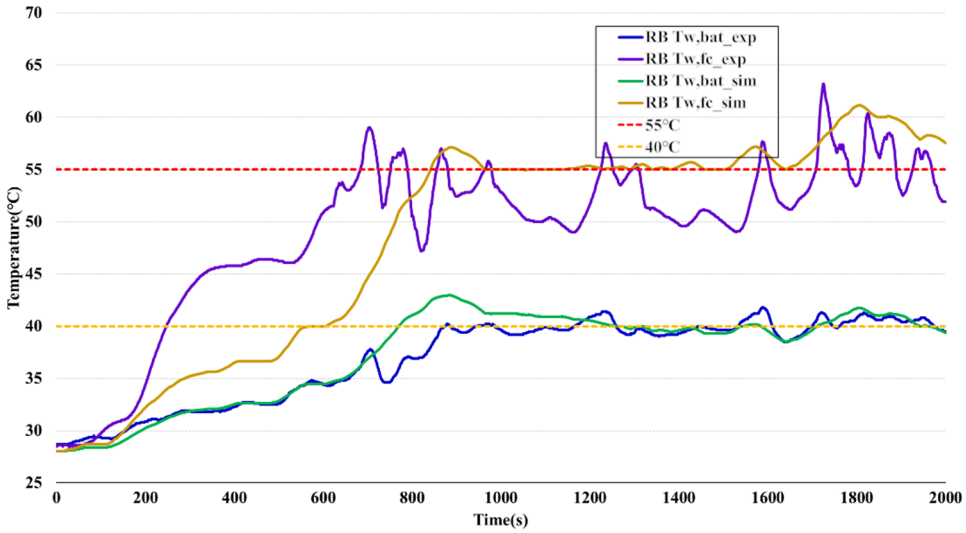

Figure 9. Simulation/experiment comparison of coolant temperature variations of two energy sources.

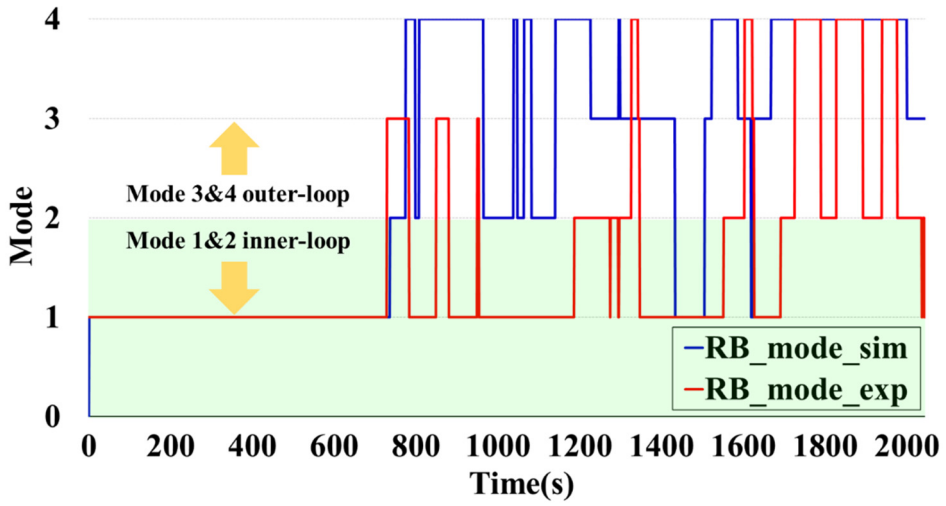

Figure 10. Simulation/experiment comparison of the mode-switch timing.

Figure 11 demonstrates the control signals of key components (proportional valve voltage, coolant pump voltage and radiator voltage) for the simulation/experiment comparison. In the beginning of the experiments, as in mode 1, the voltages of proportional valve, coolant pump, and radiator were 1.98 V, 1.7 V, and 0 V, respectively. At the 873rd second, both temperatures of dual energy sources reach targets, so that the voltages of proportional valve, coolant pump, and radiator were changed to 2.2 V, 3.83 V, and 5 V, respectively, where the targets were tracked well. In the simulation, the initial voltages of actuators were the same as those in the experiments. At the 843rd second, both temperatures of dual energy sources reach targets where there was a 30 s difference between the simulation and the experiment cases.

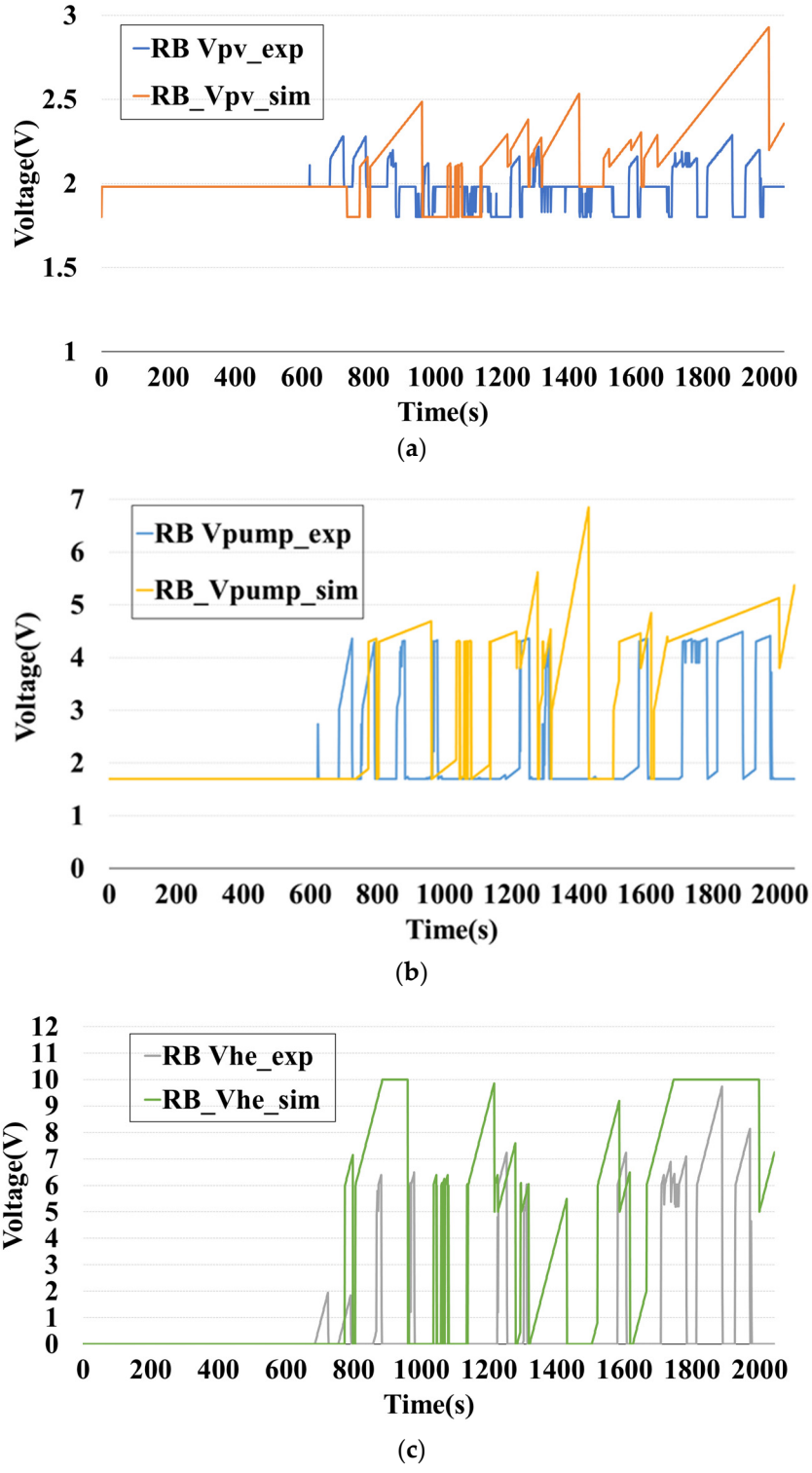

Figure 11. Simulation/experiment comparison of the control signals of key components: (**a**) proportional valve voltage; (**b**) coolant pump voltage; (**c**) radiator voltage.

From the above, it shows that the simulator is able to represent the experimental platform for further application such as: performance evaluation of system performance, thermal management system designs for various power/energy sources and advanced control strategy development for thermal management systems.

5. Conclusions

In this research, a dynamics simulator of an innovative hybrid thermal management system was constructed and the results were compared with those of a constructed experimental platform. The conclusion is summarized as follows:

(1) An ITHMS was designed: a novel configuration of a thermal management system with inner and outer-loop configuration for hybrid energy sources was developed. By governing three electromagnetic valves, a proportional valve, a coolant pump and the radiator on the heat exchanger, the optimal operation temperatures for dual sources were effectively controlled.

(2) A low-ordered lumped-parameter dynamics model was constructed: based on Newton's law of cooling and lumped-parameter technique for the control volumes defined in the system, a set of first-ordered equations was produced, where a Matlab/Simulink-based simulator was constructed.

(3) The mechatronics and supervisory system of an experimental platform was established: the inner/outer-loop thermal management system with key components as well as time-variant heating sources were constructed on the platform. The heat pipes, actuators and sensors, and harness were integrated. The important variables were supervised with the closed-loop control.

The average simulation-experiment temperature error of the battery was 0.898 °C and the average simulation-experiment temperature error of the PEMFC was 4.839 °C. It shows that the transient behavior of the simulator was similar to the experimental results of the platform. For the limitation of this research, since the waste heat was emulated and generated by the heaters and sinks, the actual thermal dynamics and detailed temperature distribution of actual energy sources cannot be analyzed. In the future, the real fuel cells and lithium batteries will be applied for the IHTMS. An electric load will draw the current to emulate the traction motor of an EV. Moreover, the verified IHTMS will be integrated to a real vehicle, while the performance will be tested on the chassis dynamometer.

Author Contributions: Conceptualization and methodology, Y.-h.H. and Y.-h.L.; theories and equation derivation, Y.-h.H., Y.-h.L. and L.-f.L.; software design and simulation, Y.-h.L. and L.-f.L.; experimental platform designs, Y.-h.H., Y.-h.L., L.-f.L. and C.-h.C.; experimental platform construction, Y.-h.L. and L.-f.L.; original draft preparation, Y.-h.H., Y.-h.L., L.-f.L. and C.-h.C.; writing, Y.-h.H. and C.-h.C. All authors have read and agreed to the published version of the manuscript.

Funding: This research received no external funding.

Institutional Review Board Statement: Not applicable.

Informed Consent Statement: Not applicable.

Acknowledgments: The authors would like to thank the Ministry of Science and Technology of the Republic of China, Taiwan, for supporting this research under Contract No. MOST 110-2221-E-003-010-MY3, and 108-2628-E-003-001.

Conflicts of Interest: The authors declare no conflict of interest.

References

1. Tostado-Véliz, M.; Arévalo, P.; Jurado, F. A comprehensive electrical-gas-hydrogen Microgrid model for energy management applications. *Energy Convers. Manag.* **2020**, *228*, 113726. [CrossRef]
2. Wang, S.; Rafiz, K.; Liu, J.; Jin, Y.; Lin, J.Y. Effects of lithium dendrites on thermal runaway and gassing of $LiFePO_4$ batteries. *Sustain. Energy Fuels.* **2020**, *4*, 2342–2351. [CrossRef]
3. Noponen, M.; Mennola, T.; Mikkola, M.; Hottinen, T.; Lund, P. Measurement of current distribution in a free-breathing PEMFC. *J. Power Sources* **2002**, *106*, 304–312. [CrossRef]
4. Hung, Y.H.; Tung, Y.M.; Chang, C.H. Optimal control of integrated energy management/mode switch timing in a three-power-source hybrid powertrain. *Appl. Energy* **2016**, *173*, 184–196. [CrossRef]
5. Hung, Y.H.; Wu, C.H. A combined optimal sizing and energy management approach for hybrid in-wheel motors of EVs. *Appl. Energy.* **2015**, *139*, 260–271. [CrossRef]

6. Hamesa, Y.; Kayaa, K.; Baltacioglub, E.; Turksoya, A. Analysis of the Control Strategies for Fuel Saving in the Hydrogen Fuel Cell Vehicles. *Int. J. Hydrog. Energy* **2018**, *43*, 10810–10821. [CrossRef]
7. Mohajer, S.; Sabatier, J.; Lanusse, P.; Cois, O. Electro-Thermal and Aging Lithium-Ion Cell Modelling with Application to Optimal Battery Charging. *Appl. Sci.* **2020**, *10*, 4038. [CrossRef]
8. Cao, W.J.; Zhao, C.R.; Wang, Y.W.; Dong, T.; Jiang, F.M. Thermal modeling of full-size-scale cylindrical battery pack cooled by channeled liquid flow. *Int. J. Heat Mass Transf.* **2019**, *138*, 1178–1187. [CrossRef]
9. Ouyang, D.; Chen, M.; Huang, Q.; Weng, J.; Wang, Z.; Wang, J. A Review on the Thermal Hazards of the Lithium-Ion Battery and the Corresponding Countermeasures. *Appl. Sci.* **2019**, *9*, 2483. [CrossRef]
10. Piotr, J.B. Identification of the Wear Margin of a Pipeline–Machine Subsystem. *Appl. Sci.* **2020**, *10*, 3977.
11. Qian, Z.; Li, Y.M.; Rao, Z.H. Thermal performance of lithium-ion battery thermal management system by using mini-channel cooling. *Energy Convers. Manag.* **2016**, *126*, 622–631. [CrossRef]
12. Xu, H.J.; Wang, J.X.; Li, Y.Z.; Bi, Y.J.; Gao, L.J. A Thermoelectric-Heat-Pump Employed Active Control Strategy for the Dynamic Cooling Ability Distribution of Liquid Cooling System for the Space Station's Main Power-Cell-Arrays. *Multimed. Tools Appl.* **2019**, *21*, 578. [CrossRef]
13. Behi, H.; Behi, M.; Karial, D.; Jagemont, J.; Ghanbarpour, M.; Behnia, M.; Berecibar, M.; Mierlo, J.V. Heat pipe air-cooled thermal management system for lithium-ion batteries: High power applications. *Appl. Therm. Eng.* **2020**, *183*, 16240. [CrossRef]
14. Tostado-Véliz, M.; León-Japa, R.S.; Jurado, F. Optimal electrification of off-grid smart homes considering flexible demand and vehicle-to-home capabilities. *Appl. Energy* **2021**, *298*, 117184. [CrossRef]
15. Kim, J.; Oh, J.; Lee, H. Review on battery thermal management system for electric vehicles. *Appl. Therm. Eng.* **2019**, *149*, 192–212. [CrossRef]
16. Hakeem, A.A.; Solyali, D. Empirical Thermal Performance Investigation of a Compact Lithium Ion Battery Module under Forced Convection Cooling. *Appl. Sci.* **2020**, *10*, 3732. [CrossRef]
17. Chen, M.; Zhang, S.; Wang, G.; Weng, J.; Ouyang, D.; Wu, X.; Zhao, L.; Wang, J. Experimental Analysis on the Thermal Management of Lithium-Ion Batteries Based on Phase Change Materials. *Appl. Sci.* **2020**, *10*, 7354. [CrossRef]
18. Hung, Y.H.; Teng, T.P.; Teng, T.C. Assessment of heat dissipation performance for nanofluid. *Appl. Therm. Eng.* **2011**, *32*, 132–140. [CrossRef]
19. Hung, Y.H.; Gu, H.J. Multiwalled Carbon Nanotube Nanofluids Used for Heat Dissipation in Hybrid Green Energy Systems. *J. Nanomater.* **2014**, *2014*, 12. [CrossRef]
20. Hung, Y.H.; Lin, Y.X.; Wu, C.H.; Chen, S.Y. Mechatronics design and experimental verification of an electric-vehicle-based hybrid thermal management system. *Adv. Mech. Eng.* **2016**, *8*, 1–9. [CrossRef]
21. Luo, L.; Jian, Q.; Huang, B.; Huang, Z.; Zhao, J.; Cao, S. Experimental study on temperature characteristics of an air-cooled proton exchange membrane fuel cell stack. *Renew. Energ.* **2019**, *143*, 1067–1078. [CrossRef]
22. Bargal, H.S.; Souby, M.M.; Abdelkareem, A.A.; Sayed, M.; Tao, Q.; Chan, M.; Wang, Y. Experimental investigation of the thermal performance of a radiator using various nanofluids for automotive PEMFC applications. *Int. J. Energy Res.* **2020**, *45*, 6831–6849. [CrossRef]
23. Gan, Y.H.; Wang, J.Q.; Liang, J.L.; Huang, Z.H.; Hu, M.L. Development of thermal equivalent circuit model of heat pipe-based thermal management system for a battery module with cylindrical cells. *Appl. Ther. Eng.* **2020**, *164*, 114523. [CrossRef]
24. Kim, S.; Jeong, H.; Lee, H. Cold-start performance investigation of fuel cell electric vehicles with heat pump-assisted thermal management systems. *Energy* **2021**, *232*, 121001. [CrossRef]
25. Hung, Y.H.; Wang, W.P.; Hsu, Y.C.; Teng, T.P. Performance evaluation of an air-cooled heat exchange system for hybrid nanofluids. *Exp. Ther. Fluid Sci.* **2017**, *81*, 43–55. [CrossRef]